

Reconstruction of internal structures and numerical simulation for concrete composites at mesoscale

Chengbin Du¹, Shouyan Jiang*¹, Wu QIN², Hairong Xu¹ and Dong Lei¹

¹Department of Engineering Mechanics, Hohai University, Nanjing 210098, China

²CCCC Third Harbor Consultants Co., Ltd, Shanghai 200032, China

(Received March 12, 2011, Revised November 3, 2011, Accepted December 19, 2011)

Abstract. At mesoscale, concrete is considered as a three-phase composite material consisting of the aggregate particles, the cement matrix and the interfacial transition zone (ITZ). The reconstruction of the internal structures for concrete composites requires the identification of the boundary of the aggregate particles and the cement matrix using digital imaging technology followed by post-processing through MATLAB. A parameter study covers the subsection transformation, median filter, and open and close operation of the digital image sample to obtain the optimal parameter for performing the image processing technology. The subsection transformation is performed using a grey histogram of the digital image samples with a threshold value of [120, 210] followed by median filtering with a 16×16 square module based on the dimensions of the aggregate particles and their internal impurity. We then select a “disk” tectonic structure with a specific radius, which performs open and close operations on the images. The edges of the aggregate particles (similar to the original digital images) are obtained using the canny edge detection method. The finite element model at mesoscale can be established using the proposed image processing technology. The location of the crack determined through the numerical method is identical to the experimental result, and the load-displacement curve determined through the numerical method is in close agreement with the experimental results. Comparisons of the numerical and experimental results show that the proposed image processing technology is highly effective in reconstructing the internal structures of concrete composites.

Keywords: digital image processing; concrete composites; mesoscale; experiment; numerical simulation.

1. Introduction

At mesoscale, concrete is considered as a three-phase composite material consisting of the aggregate particles (including both coarse and fine aggregates), the cement matrix and ITZ. Therefore, the mechanical properties of concrete composites primarily depend on its components and microstructures, and its aggregate shape, size and gradation also have a considerable effect on its properties. Due to the difficulty in acquiring the actual internal structures of concrete composites, several numerical methods (Du and Sun 2007, Xu *et al.* 2010, Leite *et al.* 2007) have been developed to generate randomly distributed aggregate particles in the cement matrix. The generation mechanism demands that the shape, size and distribution of aggregate particles resemble actual concrete composites in the statistical sense. Moreover, the numerical model assumes that the aggregate particles are composed of simple geometric bodies, that is, circular, spherical and arbitrary polygons, which are

* Corresponding author, Ph.D. Student, E-mail: syjiang@hhu.edu.cn

often significantly different from the actual aggregate particles. To apply a periodic boundary condition, the unit cell method (Ghouse *et al.* 2010) has been adopted to establish more simply the numerical model of concrete composites at mesoscale. Though the capability of those methods is apparent in analyzing the mechanical behaviour of concrete composite at mesoscale, there is a considerable gap between the numerical model and the actual case.

To acquire the actual internal structures of concrete composites at mesoscale, a new technology to model concrete close to reality has been developed by reconstructing digital images or X-ray computerized tomography (CT) image. The model can derive an approximate estimate of the actual shape and distribution of the aggregate particles to facilitate accurate characterization of the heterogeneity of the mesoscopic structure of concrete. Through comparisons of radiography, X-ray CT, infrared thermography, radar imaging and acoustic imaging methods, Buyukozturk (1998) concluded that X-ray CT was the most effective method to acquire the internal structures of concrete composites. Mora *et al.* (1998) have studied the application of digital image processing technology in the aspect of aggregate generation. John *et al.* (2001) have found that digital image correlation (DIC) technology was suitable for observing small cracks on the surface of concrete, and X-ray CT was more effective for imaging large cracks in the concrete. At the same time, they also discussed the influence of the shape of aggregate particles and the crack shape on the strength of concrete based on the X-ray CT images that are obtained after concrete fracture. Yang *et al.* (2001) have described a general method of separating the aggregate element from images using scanning electron microscopy (SEM). Yue *et al.* (2003) have developed a finite element method based on digital images and studied the effect of the shape of aggregate particles and their spatial distribution on the mechanics of mixture in asphalt concrete. To overcome the problem of close proximity and touching aggregates, Kutay *et al.* (2010) have presented the filtered watershed transform (FWT) as an alternative image processing method. Kocur *et al.* (2010) have demonstrated the synergy between X-ray CT data for a concrete specimen and numerical simulations of elastic wave propagation in a purely numerical concrete model.

Due to the significant differences in the densities of the aggregate particles, the cement matrix and the air void in the concrete material, the distribution of each component can be identified effectively using X-ray CT technology. Though the X-ray CT technology is an effective tool to investigate the internal structural characteristics of concrete, the technology is time-consuming and expensive in the aspect of investigating the internal structures of concrete composites. In addition, X-ray CT also imposes restrictions on the specimen size and shape as well as on the environment. By comparison, sectional digital images obtained using a digital camera can reflect the colour distribution of each component through a low cost and simple technique, showing its advantage in acquiring the internal structures of concrete. However, the grey value of the aggregate phase with an uneven radial distribution in the concrete has a large span, and the grey value of the cement matrix lies among the unevenly distributed phases. Thus, it is difficult to recognize the actual internal structures of concrete based directly on the digital images, some critical image processing technology are essential.

In this paper, we introduce a method of acquiring the internal structures of concrete composites through digital imaging of the concrete section and the proposed image processing technology. The method can be used to establish the numerical model of concrete at mesoscale, and the numerical and experiment results were compared to verify the validity of the proposed image processing technology.

2. Reconstruction of the internal structures for concrete composites

2.1 Digital imaging of the concrete section

In this section, we introduce the method of acquiring the internal structures of concrete composites using digital imaging of concrete sections. As shown in Fig. 1, a $100\text{ mm} \times 100\text{ mm}$ concrete section is imaged from the concrete specimen using a general digital camera. From the extracted digital image consisting of 1000 pixels by 1000 pixels, the local sample with the pixel of 460×400 is taken out as the introduction of 2D image processing method. From Fig. 1, we see that the cement matrix exhibits a single colour, whereas the aggregate particle exhibits multiple colours.

During the processing of the image, we make the following assumptions:

- (1) Concrete is considered as a two-phase composite consisting of the aggregate particles and the cement matrix. Each phase, that is, the aggregate particles and the cement matrix, is continuous and homogeneous without any air void or micro-cracks.
- (2) The coarse aggregates with pixel size greater than 100 are included, whereas the partial fine aggregates are ignored.
- (3) The errors caused by the sampling and quantizing processes are not considered.

2.2 Image processing method

2.2.1 Subsection transformation of the images

The histogram of the concrete section shown in Fig. 2(a) clearly illustrates the segmented constituents. From the histogram, we see that the grey value of the aggregate particles is distributed in $[55, 100]$, whereas the grey value of the cement matrix is distributed in $[140, 170]$. The MATLAB tool contains the function shown in Eq. (1) that can directly convert a digital image to a binary image. The threshold can be obtained as the grey value at the site of a wave trough. The remaining grey values below and above the threshold is set to 0 and 1, respectively. The binary image is shown in Fig. 2(b). From the figure, we can see substantial cavitation erosion in the

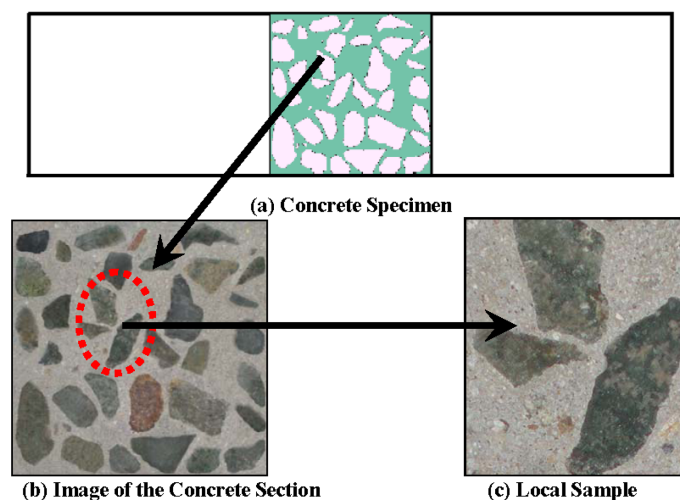


Fig. 1 Digital image of the concrete section

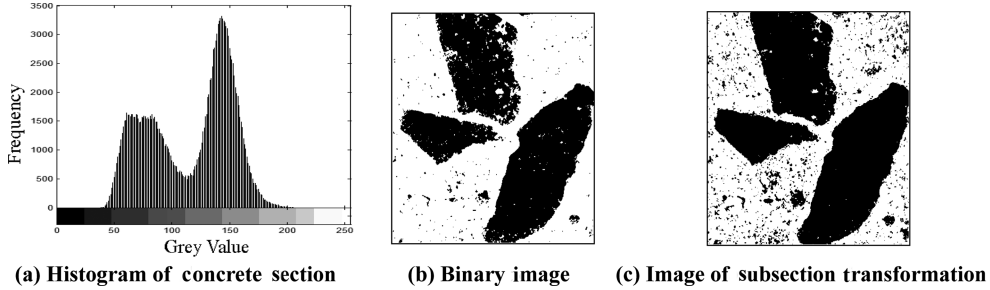


Fig. 2 Effect for images of subsection transformation

aggregate particles after the binary conversion, which may lead to the loss of boundary information. The erosion occurs due to the presence of components in the aggregate particles whose grey values lie in the range of grey value for the cement matrix. Edge detection of the aggregate particles performed using the binary image will result in considerable error in the extracted boundary. Therefore, we adopted the subsection transformation shown in Eq. (2) for the image. After the grey value range of the aggregate is identified, the grey values above or below those of the aggregates are considered as the cement matrix.

$$f(i,j) = \begin{cases} 0 & f(i,j) < \xi \\ 1 & f(i,j) \geq \xi \end{cases} \quad (1)$$

where, $f(i, j)$ is the grey value of pixel in the i th row and the j th column; ξ is the threshold of grey values between the aggregate and the cement matrix.

$$f(i,j) = \begin{cases} 0 & f(i,j) \in [\xi_1, \xi_2] \\ 1 & f(i,j) \notin [\xi_1, \xi_2] \end{cases} \quad (2)$$

where, ξ_1 and ξ_2 are the threshold of grey values between the aggregate particles and the cement matrix.

However, the grey levels of the aggregate particles in the digital image often overlap with those of the cement matrix. It should be noted that the holding of the information of aggregate particles and avoiding their cavitation erosion may introduce more noise in some parts of the cement matrix. Thus, according to the original images and the grey histogram, ξ_1 and ξ_2 are finally designated as 120 and 210, respectively. The image of the subsection transformation is shown in Fig. 2(c).

2.2.2 Filtering and elimination of noise

The effect of the electrical and mechanical noise, the environment of the screen, and the subsection transformation inevitably lead to substantial noise in the generated image. Therefore, the image of the subsection transformation must be filtered and the noise must be eliminated to remove any potential impurities in the regions corresponding to the aggregate particles and the cement matrix. Through the disposal of these potential impurities, the regions corresponding to the aggregate particles and the cement matrix can become a continuous and single-valued massive area. Therefore, the purpose of the filtering process is to recover the interior information of the two regions and to smoothen the boundary between them. In this paper, we consider the filtering method in the spatial

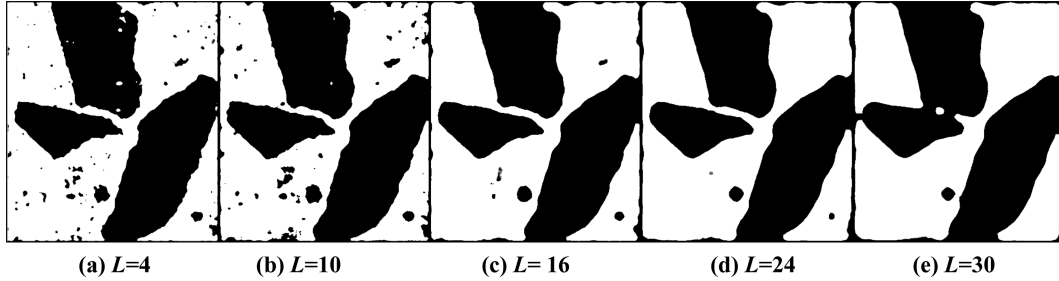


Fig. 3 Result of median filtering

domain and median filtering is selected to eliminate noise.

The principle of median filtering is that the grey value in a certain pixel, called the unit processing region, is substituted by the median pixel value of a sequence of pixels in the neighbourhood of the unit processing region. If the unit processing region is set to A , then the output of median filtering is as follows

$$f(i,j) = \text{Med}\{x_{ij}\} = \text{Med}\{x_{(i+r)(j+s)}, (r,s) \in A\} \quad (3)$$

where, $f(i,j)$ is the grey value in the i th row and the j th column; $\text{Med}\{ \}$ denotes the get median function; x_{ij} is the original grey value of each point in the digital image; and r, s are the length and width of the unit processing region A with units in pixels.

Median filtering can be explained as follows: if the unit processing region that is obtained by considering a certain point as the centre contains more aggregate elements with pixels beyond half, the point is regarded an aggregate element. The same method covers the cement matrix element. In this paper, median filtering for the images of subsection transformation has been performed using a square unit processing region with side length L measuring 4, 10, 16, 24 and 30 pixels, respectively. The results of the median filtering are shown in Fig. 3. The figure shows that $L=4$ and $L=10$ exhibit negative effects during the median filtering, and the cement matrix regions contain significant noise. Cavitation erosion is also present in the regions of the aggregate particles. When $L=30$, the superfluous information in the region of the cement matrix is removed though filtering; however, some fine aggregates disappear after median filtering. In addition, the enlargement in the boundary of the aggregate particles worsens the recognition effect. Lengths $L=16$ and $L=24$ exhibit positive effects on the noise removal; the approximate scope of the aggregate particles can be determined and the cement matrix can be smoothed. The boundary information of the fine aggregate particles is retained. However, when $L=24$, the connected scope of the aggregate particles and the boundary is enlarged, which may lead to errors during border identification. Finally, a 16×16 square module is selected as the unit processing region for median filtering based on the size of the aggregate particles and on the interior cavitation erosion situation. The result of median filtering is shown in Fig. 3(c).

2.2.3 Morphological image processing

As shown in Figs. 2(c) and 3, the impurities are present in the regions of the aggregate particles and the boundary of the aggregate particles is relatively coarse. This may be attributed to the large size of the impurity and the similarity in its colour with that of the cement matrix, and to the loss of the boundary information of the image after subsection transformation. In addition, the size of the

unit processing region during median filtering is restricted by the size of the aggregate particles. Therefore, the morphology theory is used to further handle the images.

(1) Expansion and corrosion

The morphology process based on expansion and corrosion algorithms is used to further process the images to eliminate redundant information in the image boundary. Expansion can lengthen and thicken the objects in the images; corrosion can shrink and thin these objects (Gonzalez *et al.* 2009). If the structuring element B is used to perform the expanding operation on the image f , denoted by $f \oplus B$, then the set operation can be defined as follows

$$f \oplus B = \{z | (\hat{B})_z \cap f \neq \emptyset\} \quad (4)$$

where, z is the translation amount; $(\hat{B})_z$ is the set after the mapping structuring element \hat{B} is translated by z . If the structuring element B is used to perform corrosion on the image f , denoted by $f \ominus B$, then the set operation can be defined as follows

$$f \ominus B = \{z | (B)_z \cap f^c \neq \emptyset\} \quad (5)$$

where, $(B)_z$ is the set after the structuring element B is translated by z ; f^c is the complementary set of f .

Performing expansion or corrosion directly on the image cannot solve all of the problems, and it may even introduce more errors in the boundary. Therefore, we use a combination of expansion and corrosion operations. An ‘open operation’ is defined as corrosion applied first followed by expansion through structuring elements denoted by $f \circ B$. At the same time, the object regions without structuring elements can be deleted and their contours can be smoothed. The open operation can be defined as follows

$$f \circ B = (f \ominus B) \oplus B \quad (6)$$

On the other hand, a ‘close operation’ is defined as expansion applied first followed by corrosion of the images through structuring elements denoted by $f \bullet B$. Thus, the narrow gap can be connected and the holes that are smaller than the structuring elements can also be filled. The close operation can be defined as follows

$$f \bullet B = (f \oplus B) \ominus B \quad (7)$$

(2) Influence of the structuring element “disk” radius on image processing technology

In this paper, the structuring element B is configured using the IPT function *strel* in MATLAB. First, the circular structuring element with radius R is denoted as (“disk”, R) and the radius is set to

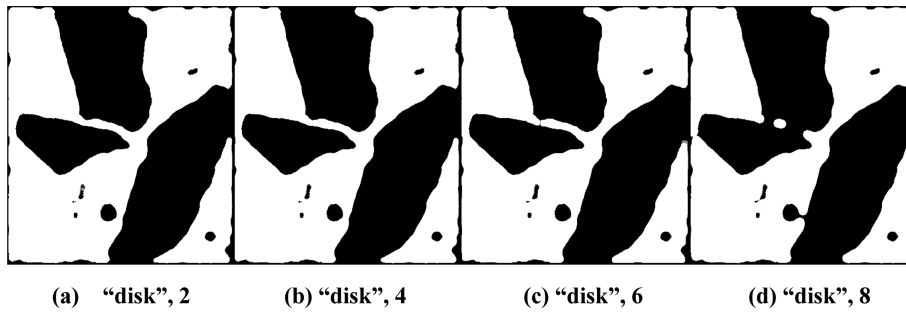


Fig. 4 Result of the open operation with different “disk” radius

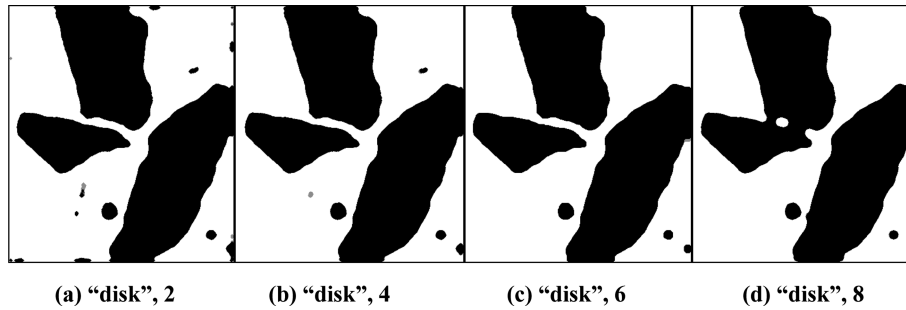


Fig. 5 Result of the close operation with different “disk” radius

2, 4, 6 and 8 pixels, respectively. The open operation is first performed on the median filtered image followed by the close operation. As shown in Figs. 4 and 5, when $R = 2$, the open and close operations show very little influence on the images, which still contain superfluous information; when $R = 8$, the regions among the aggregate particles are connected and the aggregate shape undergoes expansion, which does not comply with the actual situation; when $R = 4$ and $R = 6$, both operations exhibit satisfactory results on the identification of the shape of aggregate particles and their scope, and they selectively remove superfluous information at the edge of the images. Finally, the structuring element is configured using the “disk” with radius $R = 6$ based on the aggregate shape and size in the images.

(3) Influence of different structuring elements on image processing technology

As shown in Fig. 6, to explain the effect of the shape of the structuring element on the image processing technology, (“line”, 12, 0), (“square”, 6) and (“diamond”, 6) are selected to configure the structuring elements to perform open and close operations on the median filtered images, respectively. From Figs. 5(c) and 6, the structuring element configured by (“line”, 12, 0) exhibits a positive processing effect for vertical superfluous information, but it cannot eliminate the superfluous information on the upper and lower boundary, and small aggregates are stretched after processing; (“square”, 6) and (“diamond”, 6) can also eliminate superfluous information to determine the exact aggregate shape. However, after being processed, the fine aggregates are approximated to the square and diamond elements, respectively, and their boundaries can lead to errors due to stress concentration in the following mechanical analysis. Thus, (“disk”, 6) obtains satisfactory results for the boundary shape of the aggregate particles and simplifies the subsequent boundary identification process.

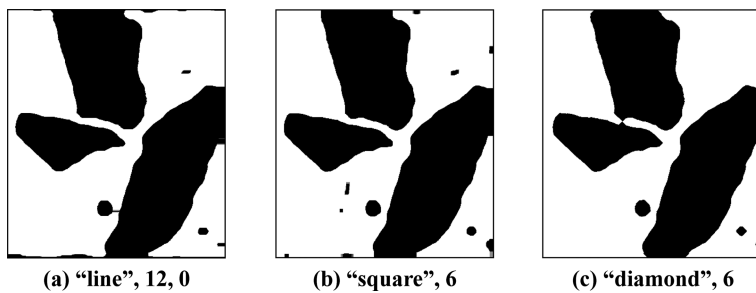


Fig. 6 Result of the close operation with different structuring elements

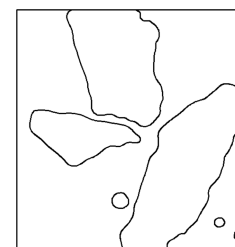


Fig. 7 Result of boundary identification

2.3 Boundary identification

According to the image processing method proposed in this paper, the superfluous information in the regions of the aggregate particles and the cement matrix is almost eliminated, and the shape of aggregate particles is separated from the original image. Then, the image boundaries can be extracted. Edge identification is performed using the canny edge detection method. As shown in Fig. 7, the edges obtained through this method retain their continuity. The identified boundary is clear, continuous and closed.

3. Numerical simulation at mesoscale

3.1 Establishment of numerical model of the specimen

The concrete specimen selected for numerical verification and simulation is different from the specimen that was used to elaborate the image processing method described in section 2. In the following section, five concrete specimens, *S-1*, *S-2*, *S-3*, *S-4* and *S-5*, divided into two groups – [*S-1*, *S-2*] for the first group and [*S-3*, *S-4*, *S-5*] for the second group – are used to experimentally investigate the initiation and propagation of the crack and the mechanical behaviour of the concrete through a four-point flexural-tension experiment.

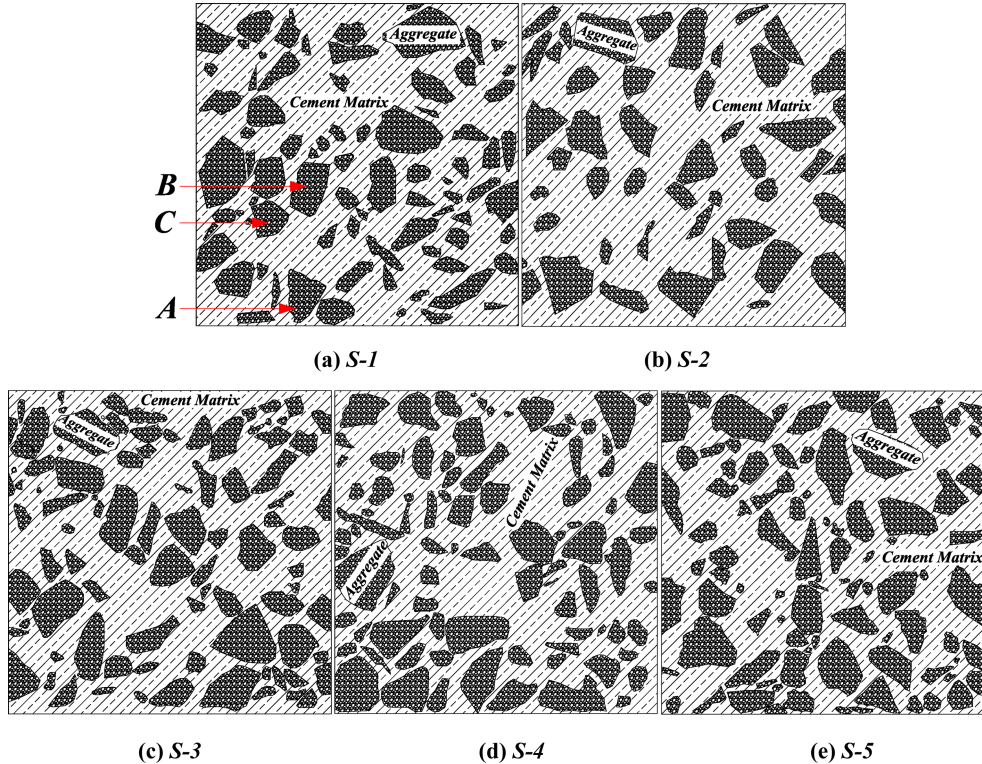


Fig. 8 Aggregate particle and cement matrix identified using the image processing technology

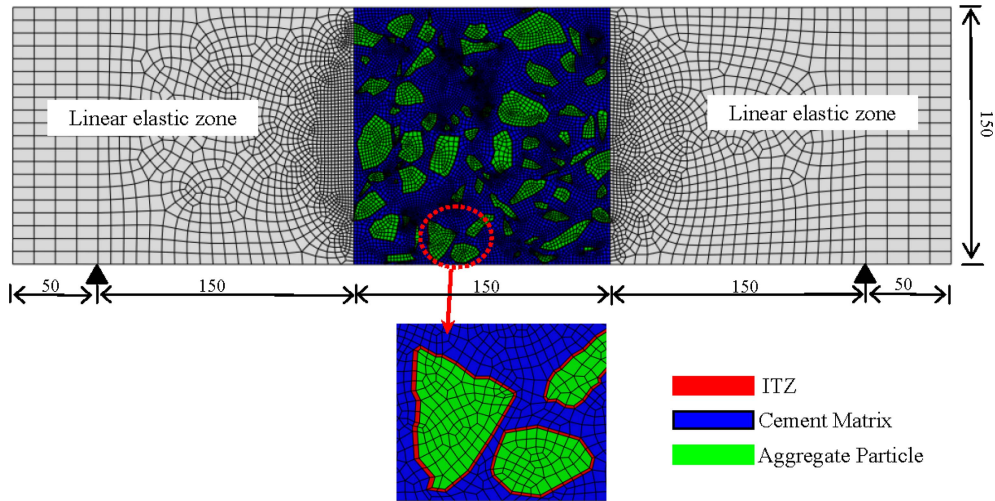


Fig. 9 Finite element mesh of specimen *S-1*/mm

The specimens in the first group are used to experimentally investigate the initiation and propagation of the crack. During the experiment, a compact high speed *S-MOTION* camera is installed to image the process of crack initiation and propagation. Therefore, no additional equipment is installed in the two specimens to precisely monitor their displacement and load. To overcome this limitation, the specimens in the second group are used to experimentally investigate the mechanical behaviour of the concrete. Therefore, the numerical model also covers the five concrete specimens. The boundary of the aggregate particles and the cement matrix of the five specimens are identified using the above-mentioned image processing technology as shown in Fig. 8.

The ITZ phase is modelled as a thin boundary layer around the aggregate and the thickness of the ITZ is assumed to be 0.5 mm. Both specimens are discretized into quadrilateral elements with 13645 nodes and 13500 elements for *S-1*, 10263 nodes and 10120 elements for *S-2*, 12646 nodes and 12519 elements for *S-3*, 12264 nodes and 12135 elements for *S-4* and 12111 nodes and 11980 elements for *S-5*. The finite element mesh of specimen *S-1* and its dimension are shown in Fig. 9, with each phase shown in different colours. All specimens are endowed with the same dimension. The thickness of these specimens is originally set to 150 mm. To capture crack initiation and propagation, both specimens are cut off at a thickness of 30 mm. To reduce the quantity of the mesh, the concern zone is considered as heterogeneous material and the remaining zones are considered as homogeneous material, that is, isotropic concrete material.

3.2 Material constitutive model

Although concrete is a type of quasi-brittle material, it is not perfectly brittle after it reaches its ultimate strength. The cohesive stress that exists in the fracture process zone must be taken into account. When reinforcement is absent in certain significant regions of the model, the tension stiffening approach introduces unreasonable mesh sensitivity in the results (Borst 2002). As shown in Fig. 10, to relieve the dependence of the simulation results on the mesh, we assume that each phase material is linearly elastic until its peak stress, and the tensile stress-crack width curve (Hillerborg *et al.* 1976) is used as a substitute for the descent segment of the stress-strain curve to

Table 1 Mechanical parameters of each component

Material zone	Elastic modulus /GPa	Poisson ratio	Tensile strength /MPa	Ultimate crack width/mm
Concrete	28	0.17	-	-
Cement matrix	22.5	0.22	3.47	0.096
Aggregate	40	0.16	5.37	0.096
ITZ	20	0.16	2.16	0.096

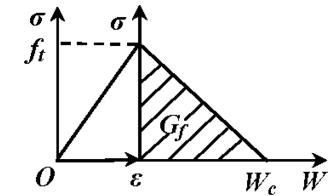
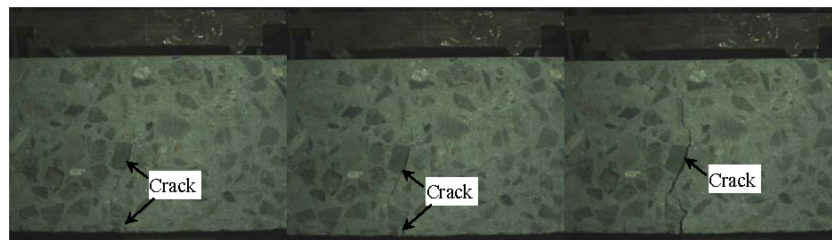


Fig. 10 Material constitutive model

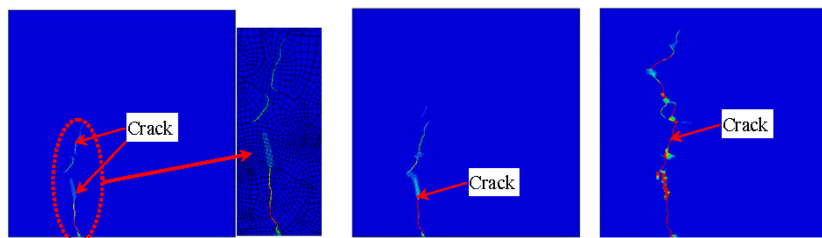
represent the strain-softening behaviour of concrete, where f_t denotes the ultimate strength of the material, G_f is the fracture energy and W_c is the limited opening displacement. The mechanical parameter of each component is shown in Table 1.

3.3 Comparison of the experimental and numerical results

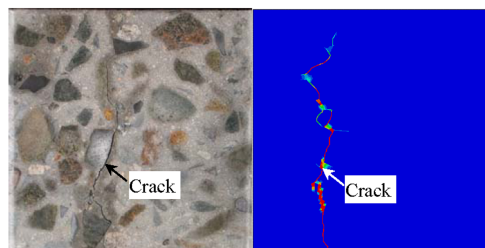
The four-point flexural-tension experiment with a static loading rate of 0.05 kN/s is performed to investigate crack initiation and propagation in the two specimens and determine their limited strength that can be obtained using a testing machine. The numerical method is also adopted to



(a) Experimental result: Crack initiation and propagation



(b) Numerical result: Crack initiation and propagation



(c) Eventual crack shape and location

Fig. 11 Specimen S-1: Comparison of experimental and numerical results

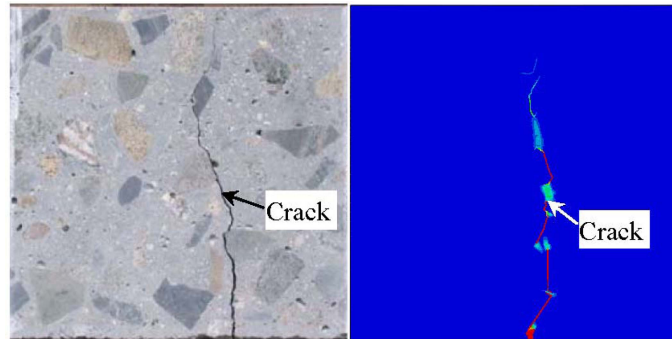


Fig. 12 Specimen *S-2*: Eventual crack shape and location obtained through the experiment and numerical methods

Table 2 Comparison of the result of the bending limit load

Specimen	Bending limit load/ kN		Error /%	$\left(\frac{ \text{Experimental result} - \text{Numerical result} }{\text{Experimental result}} \times 100\%\right)$
	Numerical result	Experimental result		
<i>S-1</i>	20.99	20.23		3.76
<i>S-2</i>	17.21	18.46		6.77

simulate the process of crack initiation and propagation based on the proposed material constitutive model. The applied load and boundary conditions agree with the experimental conditions.

For specimen *S-1*, the process of crack initiation and propagation is shown in Figs. 11(a) and (b). The experimental and numerical results both indicate that the crack is initiated at the ITZ site around the aggregate particles *A* and *B* marked in Fig. 8(a). A difference from the numerical results shows that the crack is also initiated at the ITZ site around the aggregate particle *C*. For specimen *S-2*, only the eventual crack shape and location are shown in Fig. 12 to limit the size of this paper.

As shown in Figs. 11(c) and 12, from the viewpoint of the macro scale, we see that the eventual crack shape and location obtained through the numerical and experimental methods are identical. It is observed that the fracture of the concrete composites easily initiates from the location near large aggregate in the central portion of the specimen. The investigation is quite similar to the conclusion of Bandyopadhyaya *et al.* 2008. As shown in Table 2, the bending limit load obtained through the numerical and experimental methods is also approximately equal. The crack propagates mainly along the ITZ, which is declared as the weakest zone of the concrete. Ghose *et al.* 2010 also state that initiation of failure is observed at the interface of aggregate and mortar matrix in conclusion section, but a detailed observation and discussion are absent in their studies. To arrive at the interface region, the crack must cross a part of the region corresponding to the cement matrix. However, no observations showed the fracture of the aggregate particle. The confinement of this investigation to a 2D section may have led to some internal phenomena being ignored. If we divulge the specimen at the crack site, the observation reveals that the crack propagates through a few aggregate particle. Therefore, our next work will focus on the acquisition of a 3D numerical concrete specimen (Chen 2007) and on its numerical simulation.

The specimens in the second group are then analysed to obtain their load-displacement curves. To precisely monitor the load and displacement of these specimens, the dial indicator and dynamic

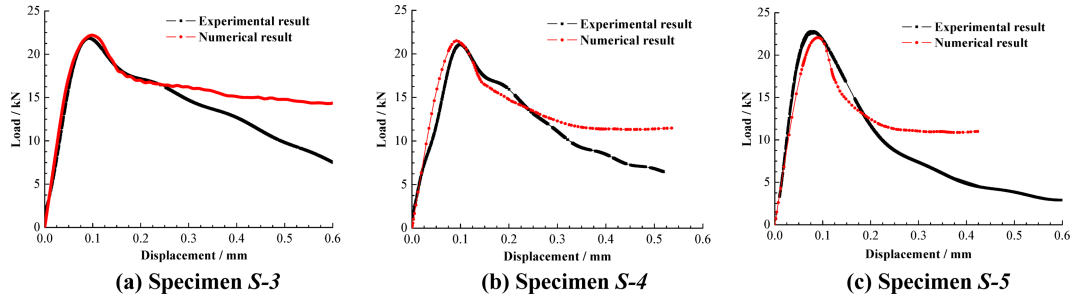


Fig. 13 Experimental and numerical results for the load-displacement curves

Table 3 Comparison of results for the bending limit load

Specimen	Bending limit load/kN		Error /%	$\left(\frac{ \text{Experimental result} - \text{Numerical result} }{\text{Experimental result}} \times 100\%\right)$
	Numerical result	Experimental result		
S-3	21.87	22.20		1.49
S-4	21.42	21.07		1.66
S-5	22.06	22.81		3.29

Table 4 Comparison of results for the elastic limit displacement

Specimen	Displacement/mm		Error /%	$\left(\frac{ \text{Experimental result} - \text{Numerical result} }{\text{Experimental result}} \times 100\%\right)$
	Numerical result	Experimental result		
S-3	0.091	0.098		7.14
S-4	0.096	0.10		4.00
S-5	0.088	0.078		12.82

strain gauge that otherwise prevent the installation of the *S*-MOTION camera are both installed. Based on the selected parameters and the proposed material constitutive model, the numerical simulation of the three specimens is also performed. As shown in Fig. 13, before the specimen reaches its peak strength, the load-displacement at the mid-span curve obtained using the numerical method is in close agreement with the experimental results, especially for specimens *S*-3 and *S*-5. After the specimens reach their peak strength, the consistent variations in these curves can still be investigated. Comparisons of numerical and experimental results for the bending limit load and the elastic limit displacement are shown in Tables 3 and 4, respectively. The error can be limited to approximately 13%.

4. Conclusions

The actual internal structures of concrete composites can be acquired by identifying the boundary of the aggregate particles and the cement matrix using digital imaging technology, that is, subsection transformation, median filtering, expansion and corrosion. The low cost and simple operation of the method shows its advantage in acquiring the actual internal structures of concrete and its wide application potential. Based on the proposed image processing technology, the numerical concrete

model can be established at mesoscale. The crack shape and location obtained using the numerical method is identical to the experimental result. The load-displacement curve obtained using the numerical method is also in close agreement with the experimental results. Comparisons of the numerical and experimental results show that the proposed image processing technology is an effective method of acquiring the actual internal structures of concrete composites.

Acknowledgements

The authors gratefully acknowledge support for this research from the National Natural Science Foundation of China (Grant Nos. 11132003 and 50779011) and the Innovative Project for graduate students of Jiangsu Province (Grant No. CX10B_202Z).

References

- Bandyopadhyaya, R., Das, A. and Basu, S. (2008), "Numerical simulation of mechanical behaviour of asphalt mix", *Constr. Build. Mater.*, **22**(6), 1051-1058.
- Borst, R. (2002), "Fracture in quasi-brittle materials: a review of continuum damage-based approach", *Eng. Fract. Mech.*, **69**(2), 95-112.
- Buyukozturk, O. (1998), "Imaging of concrete structures", *NDT&E. Int.*, **31**(4), 233-243.
- Chen, H.Q. (2007), "On the obstacles and way to assess the seismic catastrophe for high arch dams", *Sci. China Ser. E.*, **50**(1), 11-19.
- Du, C.B. and Sun, L.G. (2007), "Numerical simulation of aggregate shapes of two dimensional concrete and its application", *J. Aerospace Eng.*, **20**(3), 172-178.
- Ghouse, M.D., Lakshmana, R.C. and Rao, B.N. (2010), "Numerical simulation of fracture process in cement concrete using unit cell approach", *Mech. Adv. Mater. Struc.*, **17**(7), 481-487.
- Gonzalez, R.C., Woods, R.E. and Eddins, S.L. (2009), *Digital image processing using MATLAB*, Gatesmark Publishing.
- Hillerborg, A., Modeer, M. and Petersson, P.E. (1976), "Analysis of crack formation and crack growth in concrete by means of fracture mechanics and finite elements", *Cement Concrete Res.*, **6**(6), 773-782.
- John, S.L., Denis, T.K. and Surendra, P.S. (2001), "Measuring three-dimensional damage in concrete under compression", *ACI Mater. J.*, **98**(6), 465-475.
- Kocur, G.K., Saenger, E.H. and Vogel, T. (2010), "Elastic wave propagation in a segmented X-ray computed tomography model of a concrete specimen", *Constr. Build. Mater.*, **24**(12), 2393-2400.
- Kutaya, M.E., Arambulab, E., Gibsonc, N. and Youtcheff, J. (2010), "Three-dimensional image processing methods to identify and characterize aggregates in compacted asphalt mixtures", *Int. J. Pavement Eng.*, **11**(6), 511-528.
- Leite, J.P.B., Slowik, V. and Apel, J. (2007), "Computational model of mesoscopic structure of concrete for simulation of fracture processes", *Comput. Struct.*, **85**(17-18), 1293-1303.
- Moar, C.E., Kwana, K.H. and Chan, H.C. (1998), "Particle size distribution analysis of coarse aggregate using digital image processing", *Cement Concrete Res.*, **28**(6), 921-930.
- Xu, R., Yang, X.H., Yin, A.Y., Yang, S.F. and Ye, Y. (2010), "A three-dimensional aggregate generation and packing algorithm for modeling asphalt mixture with graded aggregate", *J. Mech.*, **26**(2), 165-171.
- Yang, R. and Buenfeld, N.R. (2001), "Binary segmentation of aggregate in SEM image analysis of concrete", *Cement Concrete Res.*, **31**(3), 437-441.
- Yue, Z.Q., Chen, S. and Tham, L.G. (2003), "Finite element modeling of geomaterials using digital image processing", *Comput. Geotech.*, **30**(5), 375-397.